Isotropic Cooper pairs with emergent sign changes in a single-layer iron superconductor

J. P. Rodriguez

Phys. Rev. B **95**, 134511 — Published 19 April 2017

DOI: 10.1103/PhysRevB.95.134511

Isotropic Cooper Pairs with Emergent Sign Changes in Single-Layer High-T_c Superconductor

J.P. Rodriguez[1]

[1]*Department of Physics and Astronomy,*

California State University, Los Angeles, California 90032

Abstract

We model a single layer of heavily electron-doped FeSe by spin-1/2 moments over a square lattice of iron atoms that include the $3d_{xz}$ and $3d_{yz}$ orbitals, at strong on-site Coulomb repulsion. Above half filling, we find emergent hole bands below the Fermi level at the center of the one-iron Brillouin zone in a half metal state characterized by hidden magnetic order and by electron-type Fermi surface pockets at wavenumbers that double the unit cell along the principal axes. "Replicas" of the emergent hole bands exist at lower energy in the two-iron Brillouin zone. Exact calculations with two mobile electrons find evidence for isotropic Cooper pairs that alternate in sign between the electron bands and the emergent hole bands.

Introduction. The discovery of superconductivity in iron-pnictide materials has uncovered a new path in the search for high-temperature superconductors[1]. Superconductivity has been observed recently in a single layer of FeSe on a doped $SrTiO_3$ (STO) substrate[2–4] below critical temperatures as high as 100 K [5]. Electronic conduction originates from the $3d$ orbitals of the iron atoms, which form a square lattice. Angle-resolved photo-emission spectroscopy(ARPES), in particular, reveals circular electron-type Fermi surface pockets centered at wave numbers $(\pi/a)\hat{\boldsymbol{x}}$ and $(\pi/a)\hat{\boldsymbol{y}}$ that lie along the principal axes of the iron lattice, where a is the lattice constant[6, 7]. Unlike the case of most iron-pnictide materials, however, ARPES also finds that hole bands centered at zero two-dimensional (2D) momentum lie well below the Fermi level in the case of single-layer FeSe/STO. At low temperature, it also finds an isotropic gap at the electron Fermi surface pockets[8, 9], which is confirmed by scanning tunneling microscopy (STM)[10]. The same set of phenomena have been recently observed below critical temperatures in the range 40-50 K at the surfaces of intercalated FeSe[11–13], of alkali-metal dosed FeSe[14–17], and of voltage-gate tuned thin films of FeSe[18, 19]. Comparison with bulk FeSe, which has a much lower critical temperature of 8 K, strongly suggests that the high-temperature superconductivity exhibited above is due to a new 2D groundstate that appears after heavy electron doping.

Calculations based on the independent-electron approximation[20] fail to describe the Fermi surfaces in single-layer FeSe/STO. In particular, density-functional theory (DFT) typically predicts that the hole bands centered at zero 2D momentum cross the Fermi level[8, 11, 21]. DFT also fails to account for a nearby Mott insulator phase at low electron doping in voltage-gate tuned thin films of FeSe and in single-layer FeSe/STO[19, 22]. The previous suggests that the limit of strong electron-electron interactions[23, 24] is a better starting point to describe superconductivity in heavily electron-doped FeSe.

Below, we propose that the hole bands observed by ARPES below the Fermi level at the Brillouin zone center in a surface layer of FeSe are examples of emergent phenomena. The latter is revealed by both mean-field and exact calculations of the one-electron spectrum in a two-orbital t-J model that includes only degenerate d_{xz} and d_{yz} electron bands centered at wavenumbers $(\pi/a)\hat{\boldsymbol{y}}$ and $(\pi/a)\hat{\boldsymbol{x}}$, respectively, in the one-iron Brillouin zone. Local spin-1/2 moments live on $d_{(x\pm iy)z}$ orbitals, on the other hand, which yields isotropic magnetism. Emergent hole bands approach the Fermi level at zero 2D momentum as Hund coupling increases inside of a half metal phase that is characterized by hidden Néel order per $d_{(x\pm iy)z}$

orbital and by electron-type Fermi surface pockets (inset to Fig. 1b). Emergent hole bands at wavenumber $(\pi/a)(\hat{\boldsymbol{x}} + \hat{\boldsymbol{y}})$ in the one-iron Brillouin zone are also predicted, but they lie below the former ones in energy. It is important to point out that one-electron tight-binding models that include d_{xz}, d_{yz}, and up to d_{xy} iron orbitals are unable to account for buried hole bands at the center *and* at the corner of the one-iron Brillouin zone. (Cf. refs. [25] and [26].) Last, exact calculations of two mobile electrons in the two-orbital t-J model find evidence for isotropic Cooper pairs on both the electron pockets and on the emergent hole bands below the Fermi level as Hund coupling approaches a quantum critical point (QCP) at which commensurate spin-density wave (cSDW) nesting begins. The sign of the Cooper pair wavefunction notably alternates between the electron and hole bands[27, 28].

Local Moment Model. Our starting point is a two-orbital t-J model over the square lattice, where the on-site-orbital energy cost U_0 tends to infinity[29, 30]:

$$H = \sum_{\langle i,j\rangle}[-(t_1^{\alpha,\beta}\tilde{c}^\dagger_{i,\alpha,s}\tilde{c}_{j,\beta,s} + \text{h.c.}) + J_1^{\alpha,\beta}\boldsymbol{S}_{i,\alpha}\cdot\boldsymbol{S}_{j,\beta}] + \sum_{\langle\langle i,j\rangle\rangle} J_2^{\alpha,\beta}\boldsymbol{S}_{i,\alpha}\cdot\boldsymbol{S}_{j,\beta} + \sum_i\big(J_0\boldsymbol{S}_{i,d-}\cdot\boldsymbol{S}_{i,d+} + U_0'\bar{n}_{i,d+}\bar{n}_{i,d-}\big). \quad (1)$$

Above, $\boldsymbol{S}_{i,\alpha}$ is the spin operator that acts on spin $s_0 = 1/2$ states of $d- = d_{(x-iy)z}$ and $d+ = d_{(x+iy)z}$ orbitals α in iron atoms at sites i. Repeated orbital and spin indices in the hopping and Heisenberg exchange terms above are summed over. Nearest neighbor and next-nearest neighbor Heisenberg exchange across the links $\langle i,j\rangle$ and $\langle\langle i,j\rangle\rangle$ is controlled by exchange coupling constants $J_1^{\alpha,\beta}$ and $J_2^{\alpha,\beta}$, respectively. Hopping of an electron in orbital α to a nearest-neighbor orbital β is controlled by the matrix element $t_1^{\alpha,\beta}$. We adopt the Schwinger-boson (b) slave-fermion (f) representation for the creation operator of the correlated electron[31–33] at or *above* half filling: $\tilde{c}^\dagger_{i,\alpha,s} = f^\dagger_{i,\alpha}b_{i,\alpha,s}$ with the constraint

$$2s_0 = b^\dagger_{i,\alpha,\uparrow}b_{i,\alpha,\uparrow} + b^\dagger_{i,\alpha,\downarrow}b_{i,\alpha,\downarrow} + f^\dagger_{i,\alpha}f_{i,\alpha} \quad (2)$$

enforced at each site-orbital to impose the $U_0 \to \infty$ limit on electrons with spin $s_0 = 1/2$. Finally, J_0 is a ferromagnetic exchange coupling constant that imposes Hund's Rule, while the last term in (1) represents the additional energy cost of a fully occupied iron atom. Here $\bar{n}_{i,\alpha} = \sum_s \tilde{c}^\dagger_{i,\alpha,s}\tilde{c}_{i,\alpha,s} - 1$ counts singlet pairs at site-orbitals. Last, notice that $d\pm \to e^{\pm i\theta}d\pm$ is equivalent to a rotation of the orbitals by an angle θ about the z axis. Spin and occupation operators remain invariant under it. Magnetism described by the two-orbital t-J model (1) is hence isotropic, which suppresses orbital order.

Semi-classical calculations of the Heisenberg model that corresponds to (1) at half filling find a QCP that separates a cSDW at strong Hund coupling from a hidden antiferromagnet at weak Hund coupling when diagonal frustration is present[34]: e.g. $J_1^{\parallel} > 0$, $J_1^{\perp} = 0$, and $J_2^{\parallel} = J_2^{\perp} > 0$. Here, $\parallel$ and $\perp$ represent intra-orbital ($d \pm d\pm$) and inter-orbital ($d \pm d\mp$) superscripts. The hidden-order magnet shows Néel spin order per $d\pm$ orbital following the inset to Fig. 1a. Ideal hopping of electrons within an antiferromagnetic sublattice, $t_1^{\parallel} = 0$ and $t_1^{\perp}(\hat{\boldsymbol{x}}) = -t_1^{\perp}(\hat{\boldsymbol{y}}) > 0$, leaves such hidden magnetic order intact in the semi-classical limit, $s_0 \to \infty$. Below, we employ a mean-field approximation of (1) and (2) to study this state near the QCP. It reveals a half metal with circular Fermi surface pockets at wavenumbers $(\pi/a)\hat{\boldsymbol{x}}$ and $(\pi/a)\hat{\boldsymbol{y}}$, for electrons in the d_{yz} orbital and d_{xz} orbital, respectively.

Spin-Fluctuations, One-Electron Spectrum. Following Arovas and Auerbach[31], we first rotate the spins quantized along the z axis on *one* of the antiferromagnetic sublattices shown in the inset to Fig. 1a by an angle π about the y axis. This decouples the up and down spins between the two sublattices[35]. We next define mean fields that are set by the pattern of antiferromagnetic versus ferromagnetic pairs of neighboring spins[31] in the hidden magnetic order: $Q_0 = \langle b_{i,d-,s} b_{i,d+,s} \rangle$, $Q_1^{\parallel} = \langle b_{i,d\pm,s} b_{j,d\pm,s} \rangle$ and $Q_2^{\perp} = \langle b_{i,d\pm,s} b_{j,d\mp,s} \rangle$ on the antiferromagnetic links versus $Q_1^{\perp} = \langle b^{\dagger}_{i,d\pm,s} b_{j,d\mp,s} \rangle$ and $Q_2^{\parallel} = \langle b^{\dagger}_{i,d\pm,s} b_{j,d\pm,s} \rangle$ on the ferromagnetic links of the hidden Néel state. Subscripts 0, 1 and 2 represent on-site, nearest neighbor and next-nearest neighbor links. We add to that list the mean field $P_1^{\perp} = \frac{1}{2} \langle f^{\dagger}_{i,d\pm} f_{j,d\mp} \rangle$ for nearest-neighbor hopping of electrons across the two orbitals. It has d-wave symmetry. The corresponding mean-field approximation for the t-J model Hamiltonian (1) then has the form $H_b + H_f$, where

$$H_b = \frac{1}{2} \sum_k \sum_s \{ \Omega_{fm}(k) [b_s^{\dagger}(k) b_s(k) + b_s(-k) b_s^{\dagger}(-k)] + \Omega_{afm}(k) [b_s^{\dagger}(k) b_s^{\dagger}(-k) + b_s(-k) b_s(k)] \}$$

is the Hamiltonian for free Schwinger bosons, and where $H_f = \sum_k \varepsilon_f(k) f^{\dagger}(k) f(k)$ is the Hamiltonian for free slave fermions. Here, $k = (k_0, \boldsymbol{k})$ is the 3-momentum for these excitations, where the quantum numbers $k_0 = 0$ and π represent even and odd superpositions of the $d-$ and $d+$ orbitals: d_{xz} and $(-i)d_{yz}$.

Enforcing the infinite-U_0 constraint (2) on average over the bulk then results in ideal Bose-Einstein condensation (BEC) of the Schwinger bosons into degenerate groundstates at $k = 0$ and $(\pi, \pi/a, \pi/a)$ in the zero-temperature limit: $\langle b_{i,d\pm,s} \rangle = s_0^{1/2}$ at large s_0. (See Fig. 1a and supplemental Fig. S1.) In such case, all five mean fields among the Schwinger bosons

therefore take on the unique value $Q = s_0$ [35]. This results in diagonal and off-diagonal Hamiltonian matrix elements

$$\begin{aligned}\Omega_{fm}(k) &= (1-x)^2 s_0 (J_0 + 4J_1^{\parallel} + 4J_2^{\perp} \\ &\quad -4J_1''^{\perp}[1 - e^{ik_0}\gamma_{1+}(\boldsymbol{k})] - 4J_2^{\parallel}[1-\gamma_2(\boldsymbol{k})]) \\ \Omega_{afm}(k) &= -(1-x)^2 s_0 [J_0 e^{ik_0} + 4J_1^{\parallel}\gamma_{1+}(\boldsymbol{k}) + 4J_2^{\perp} e^{ik_0}\gamma_2(\boldsymbol{k})]\end{aligned}$$

for free Schwinger bosons, and the energy eigenvalues $\varepsilon_f(k) = -8s_0 t_1^{\perp}(\hat{\boldsymbol{x}})e^{ik_0}\gamma_{1-}(\boldsymbol{k})$ for free slave fermions. Above, $J_1''^{\perp} = J_1^{\perp} - 2t_1^{\perp}(\hat{\boldsymbol{x}})P_1^{\perp}(\hat{\boldsymbol{x}})/(1-x)^2 s_0$, while $\gamma_{1\pm}(\boldsymbol{k}) = \frac{1}{2}(\cos k_x a \pm \cos k_y a)$ and $\gamma_2(\boldsymbol{k}) = \frac{1}{2}(\cos k_+ a + \cos k_- a)$, with $k_\pm = k_x \pm k_y$. Slave fermions in d_{xz} and d_{yz} orbitals lie within circular Fermi surfaces centered at wavenumbers $(\pi/a)\hat{\boldsymbol{y}}$ and $(\pi/a)\hat{\boldsymbol{x}}$, respectively, with Fermi wave vector $k_F a = (4\pi x)^{1/2}$ at low electron doping per iron orbital, $x \ll 1$. (See the inset to Fig. 1b.) The mean inter-orbital electron hopping amplitude is then approximately $P_1^{\perp}(\hat{\boldsymbol{x}}) = x/2$.

The dynamical spin correlation function $\langle S_y S'_y\rangle$ is obtained directly from the above Schwinger-boson-slave-fermion mean field theory. It is given by an Auerbach-Arovas expression at non-zero temperature that is easily evaluated in the zero-temperature limit [30, 36], where ideal BEC of the Schwinger bosons into the degenerate groundstates at 3-momenta $k = 0$ and $(\pi, \pi/a, \pi/a)$ occurs. It is one half the transverse spin correlator, which under ideal BEC and at large s_0 reads

$$i\langle S^{(+)}S'^{(-)}\rangle|_{k,\omega} = (1-x)^2 s_0 (\Omega_+/\Omega_-)^{1/2}([\omega_b(k)-\omega]^{-1} + [\omega_b(k)+\omega]^{-1}). \qquad (3)$$

Here, $\omega_b = (\Omega_{fm}^2 - \Omega_{afm}^2)^{1/2}$ is the energy dispersion of the Schwinger bosons, and $\Omega_\pm = \Omega_{fm} \pm \Omega_{afm}$. Figure 1a depicts the imaginary part of the transverse susceptibility (3) in the true spin channel, $k_0 = 0$, at sub-critical Hund coupling. It reveals a spin gap at cSDW wave numbers $(\pi/a)\hat{\boldsymbol{x}}$ and $(\pi/a)\hat{\boldsymbol{y}}$ of the form $\Delta_{cSDW} = (1-x)^2(2s_0)(4J_2^{\perp} - J_{0c})^{1/2}\mathrm{Re}\,(J_0 - J_{0c})^{1/2}$. Here, $-J_{0c} = 2(J_1^{\parallel} - J_1^{\perp}) - 4J_2^{\parallel} + (1-x)^{-2}s_0^{-1}2t_1^{\perp}(\hat{\boldsymbol{x}})x$ is the critical Hund coupling at which $\Delta_{cSDW} \to 0$. Notice that inter-orbital hopping stabilizes the hidden half metal state. The autocorrelator of the hidden spin $\boldsymbol{S}_{i,d-} - \boldsymbol{S}_{i,d+}$, (3) at $k_0 = \pi$, also shows the above spin gap at cSDW momenta, Δ_{cSDW}, in addition to a hidden-order Goldstone mode at Néel wavenumber $(\pi/a)(\hat{\boldsymbol{x}} + \hat{\boldsymbol{y}})$[35].

The electronic structure of the hidden half metal state can also be obtained directly from the above Schwinger-boson-slave-fermion mean field theory. In particular, the one-electron

propagator is given by the convolution of the conjugate propagator for Schwinger bosons with the propagator for slave fermions in 3-momentum and in frequency. A summation of Matsubara frequencies yields the expression[35]

$$G(k,\omega) = \frac{1}{\mathcal{N}} \sum_{q} \quad \Big[\Big(\tfrac{1}{2} \frac{\Omega_{fm}}{\omega_b} \Big|_{q-k} + \tfrac{1}{2} \Big) \frac{n_B[\omega_b(q-k)] + n_F[\varepsilon_f(q) - \mu]}{\omega + \omega_b(q-k) - \varepsilon_f(q) + \mu}$$
$$+ \Big(\tfrac{1}{2} \frac{\Omega_{fm}}{\omega_b} \Big|_{q-k} - \tfrac{1}{2} \Big) \frac{n_B[\omega_b(q-k)] + n_F[\mu - \varepsilon_f(q)]}{\omega - \omega_b(q-k) - \varepsilon_f(q) + \mu} \Big]. \qquad (4)$$

Above, n_B and n_F denote the Bose-Einstein and the Fermi-Dirac distributions, and μ denotes the chemical potential of the slave fermions. Ideal BEC of the Schwinger bosons at 3-momenta $q - k = 0$ and $(\pi, \pi/a, \pi/a)$ results in the following coherent contribution to the electronic spectral function at zero temperature and at large s_0: $\mathrm{Im}\, G_{\mathrm{coh}}(k,\omega) = s_0 \pi \delta[\omega + \mu - \varepsilon_f(k)]$. It reveals degenerate electron bands for d_{xz} and d_{yz} orbitals centered at cSDW wave numbers $\boldsymbol{Q}_0 = (\pi/a)\hat{\boldsymbol{y}}$ and $\boldsymbol{Q}_\pi = (\pi/a)\hat{\boldsymbol{x}}$, respectively. The electron Fermi surface pockets at $\omega = 0$ are depicted by the inset to Fig. 1b. At energies below the Fermi level, $\omega < 0$, the remaining contribution is exclusively due to the first fermion term in (4). Inspection of Fig. 1b (solid lines) yields the following expression for it in the limit near half-filling, $k_F a \to 0$, at large t/J [37]:

$$\mathrm{Im}\, G_{\mathrm{inc}}(k,\omega) \cong \sum_{q_0 = 0, \pi} \frac{\pi}{2} x \left[\frac{1}{2} + \frac{1}{2} \frac{\Omega_{fm}}{\omega_b} \Big|_{(q_0 - k_0, \boldsymbol{Q}_{q_0} - \boldsymbol{k})} \right] \delta[\omega + \epsilon_F + \omega_b(q_0 - k_0, \boldsymbol{Q}_{q_0} - \boldsymbol{k})]. \qquad (5)$$

Figure 1b displays the emergent hole bands predicted above. They lie $\epsilon_F + \Delta_{cSDW}$ below the Fermi level, with degenerate maxima at $\boldsymbol{k} = 0$ and $(\pi/a)(\hat{\boldsymbol{x}} + \hat{\boldsymbol{y}})$. Here, $\epsilon_F = (2s_0) t_1^{\perp}(\hat{\boldsymbol{x}})(k_F a)^2$ is the Fermi energy. The emergent hole bands also show intrinsic broadening in frequency at zero temperature, which makes them incoherent. Outside the critical region, at large t/J, the broadening is $\Delta\omega \sim k_F |\boldsymbol{\nabla} \omega_b|_{\boldsymbol{Q} - \boldsymbol{k}}$. It remains small at the previous maxima[38]. Last, the emergent hole bands predicted by (5) are anisotropic: e.g., the d_{yz} hole band at zero 2D momentum has mass anisotropy $|m_x| < |m_y|$. (Cf. ref. [39].)

Adding intra-orbital electron hopping, $t_1^{\parallel} > 0$, brings the emergent hole bands at wavenumber $(\pi/a)(\hat{\boldsymbol{x}} + \hat{\boldsymbol{y}})$ down in energy below the ones at zero 2D momentum. This is confirmed by exact calculations of the two-orbital t-J model with one electron more than half filling over a 4×4 lattice of iron atoms under periodic boundary conditions. The previous Schwinger-boson-slave-fermion description (2) for spin $s_0 = 1/2$ electrons is exploited to impose strong on-site-orbital Coulomb repulsion. Details are given in ref. [30]. Figure

2a shows the exact spectrum at the QCP, where $\Delta_{cSDW} \to 0$. The t-J model parameters coincide with those set by Fig. 1, but with $t_1^{\parallel} = 2\,J_1^{\parallel}$, and with Hund coupling tuned to the critical value $-J_0 = 1.733\,J_1^{\parallel}$. Red states have even parity under orbital swap, $P_{d,\bar{d}}$, while blue states have odd parity under it. Notice that the lowest-energy doubly-degenerate states at wave number $(\pi/a)(\hat{\boldsymbol{x}} + \hat{\boldsymbol{y}})$, which are spin-1/2, lie $0.5\,J_1^{\parallel}$ in energy above the doubly-degenerate spin-1/2 groundstates at zero 2D momentum. The latter states (purple) move up in energy off the Fermi level set by the groundstates at cSDW momenta as Hund coupling falls below the critical value, and they become nearly degenerate with the former states in the absence of Hund's Rule. This dependence on Hund coupling is demonstrated by the inset to Fig. 2a and by supplemental Fig. S3. The exact low-energy spectrum at sub-critical Hund coupling is therefore consistent with the emergent hole bands obtained by the meanfield approximation, Fig. 1b, but with the hole bands centered at wavenumber $(\pi/a)(\hat{\boldsymbol{x}} + \hat{\boldsymbol{y}})$ pulled down to lower energy. Last, Fig. 2a shows that the even parity (d_{xz}) and odd parity (d_{yz}) spin-1/2 groundstates at wavenumber $(\pi/2a)\hat{\boldsymbol{x}}$ are nearly degenerate, which suggests isotropic emergent hole bands at zero 2D momentum near the QCP.

Cooper Pairs. Figure 2b shows the spectrum of the same two-orbital t-J model (1), but with two electrons more than half filling. A *repulsive* interaction has been added to the Heisenberg exchange terms in order to reduce finite-size effects: $\boldsymbol{S}_{i,\alpha} \cdot \boldsymbol{S}_{j,\beta} \to \boldsymbol{S}_{i,\alpha} \cdot \boldsymbol{S}_{j,\beta} + \frac{1}{4} n_{i,\alpha} n_{j,\beta}$, equal to 1/2 the spin-exchange operator. Here, $n_{i,\alpha}$ counts the net occupation of *holes* per site-orbital. Also, the on-site repulsion between mobile electrons in the $d+$ and $d-$ orbitals, respectively, is set to a large value $U_0' = \frac{1}{4} J_0 + 1000\,J_1^{\parallel}$. The Schwinger-boson-slave-fermion description of the correlation electron (2) is again employed, with $s_0 = 1/2$. Details are given in ref. [40]. Last, the ferromagnetic Hund's Rule exchange coupling constant is tuned to the critical value $J_0 = -2.25\,J_1^{\parallel}$, at which $\Delta_{cSDW} \to 0$. This is depicted by the dashed horizontal line in Fig. 2b, which shows the degeneracy between the cSDW spin resonance at wavenumber $(\pi/a)\hat{\boldsymbol{x}}$ with the hidden-order spin resonance at wavenumber $(\pi/a)(\hat{\boldsymbol{x}} + \hat{\boldsymbol{y}})$. The former is even (black) under swap of the orbitals, $d- \leftrightarrow d+$, while latter is odd (red) under it. Notice that the groundstate and the second excited state both lie under a continuum of states at zero net momentum. They respectively have even and odd parity under a reflection about the x-y diagonal. We therefore assign S symmetry to the groundstate bound pair and $D_{x^2-y^2}$ symmetry to the excited-state bound pair. The dependence of the energy-splitting between these two states on Hund coupling is shown by

the inset to Fig. 2b. It provides evidence for a true QCP in the thermodynamic limit at $-J_0 = 2.30\, J_1^{\parallel}$, where the s-wave and d-wave bound states become degenerate.

Figure 3 depicts the order parameters for superconductivity of the two bound pair states shown in Fig. 2b:

$$iF(k_0, \boldsymbol{k}) = \langle \Psi_{\rm Mott} | \tilde{c}_{\uparrow}(k_0, \boldsymbol{k}) \tilde{c}_{\downarrow}(k_0, -\boldsymbol{k}) | \Psi_{\rm Cooper} \rangle \tag{6}$$

times $\sqrt{2}$, with $\tilde{c}_s(k_0, \boldsymbol{k}) = \mathcal{N}^{-1/2} \sum_i \sum_{\alpha=0,1} e^{-i(k_0\alpha + \boldsymbol{k}\cdot\boldsymbol{r}_i)} \tilde{c}_{i,\alpha,s}$. Here, $\langle \Psi_{\rm Mott}|$ denotes the critical antiferromagnetic state of the corresponding Heisenberg model[34] at $-J_{0c} = 1.35\, J_1^{\parallel}$. (See supplemental Fig. S4.) The groundstate has S symmetry, as expected, but it also alternates in sign between Cooper pairs at electron Fermi surface pockets versus Cooper pairs at the emergent hole bands. (See Fig. 1b.) Figure 3 also shows that the (second) excited state has $D_{x^2-y^2}$ symmetry, as expected, and that it alternates in sign in a similar way. The present exact results therefore provide evidence for remnant pairing on the emergent hole bands that lie below the Fermi level at zero 2D momentum.

Discussion and Conclusions. The electronic structure in single-layer FeSe/STO is qualitatively described by the combination of Figs. 1b and 2a. For example, a fit of inelastic neutron scattering data in iron-pnictide superconductors to the true linear spinwave spectrum Fig. 1a, but at the QCP, yields $J_1^{\parallel} \cong 110$ meV, $J_1^{\perp} = 0$, and $J_2^{\parallel} \cong 40$ meV $\cong J_2^{\perp}$ for the Heisenberg exchange coupling constants[34]. Hopping parameters set in Figs. 1b and 2a imply that the bottom of the electron bands lies $\epsilon_F \cong 60$ meV below the Fermi level. Also, the cSDW spin gap displayed by Fig. 1a at sub-critical Hund coupling is approximately 50 meV, which therefore implies that the emergent hole bands at zero 2D momentum lie 110 meV below the Fermi. Both energy levels are roughly consistent with ARPES in single-layer FeSe/STO[6]. Last, the mean-field and exact spectra displayed by Figs. 1b and 2a predict that "replicas" of the d_{xz}/d_{yz} buried hole bands exist at the corner of the one-iron Brillouin zone, but with orbital quantum numbers interchanged and at lower energy. A substrate leads to two inequivalent iron atoms per hopping of electrons in d_{xz} and d_{yz} orbitals to neighboring sites. Zone-folding of the "replica" bands at lower energy to the center of the two-iron Brillouin zone possibly accounts for the "D' replicas" of the buried hole bands that are observed by ARPES on FeSe/STO[9].

Figure 3 predicts s-wave Cooper pairs on the electron Fermi surface pockets at cSDW momenta. This is consistent with ARPES and with STM on heavily electron-doped surfaces of FeSe, which find a gap on the electron Fermi surface pockets, and no evidence for

nodes[8, 10, 11, 13, 16, 17]. Notably absent from our local moment model (1) is the $3d_{xy}$ electron orbital of the iron atom. DFT calculations predict inner and outer electron Fermi surface pockets at the corner of the two-iron Brillouin zone that have d_{xz}/d_{yz} and d_{xy} orbital character, respectively[20]. In such case, the limit of strong on-site Coulomb repulsion assumed here would require remnant s-wave pairing of opposite sign on the buried d_{xy} band at the center of the Brillouin zone. The spectral weight of this band is negligibly small compared to that of the buried d_{xz}/d_{yz} hole bands according to high-resolution ARPES on alkali-metal dosed FeSe[16], however. This contradiction argues that the iron $3d_{xy}$ orbital does not play an important role in high-temperature superconductivity shown at surface layers of heavily electron-doped FeSe.

Figure 3 also predicts remnant Cooper pairs of opposite sign on the emergent hole bands that lie below the Fermi level at zero 2D momentum. The remnant pairs are possibly a result of the intrinsic broadening in frequency experienced by the emergent holes. (Cf. ref. [41].) Recent quasi-particle interference patterns obtained from surface layers of intercalated FeSe observe a feature at cSDW wavenumbers that could be accounted for by the superposition of an electron near cSDW momenta with an Andreev reflected hole near zero 2D momentum[13]. Remnant hole pairing can be confirmed in this way.

The author thanks Brent Andersen, Richard Roberts and Timothy Sell for technical help with the use of the shared-memory machine (Predator) at the AFRL DoD Supercomputing Resource Center. This work was supported in part by the US Air Force Office of Scientific Research under grant no. FA9550-13-1-0118 and by the National Science Foundation under PREM grant no. DMR-1523588.

---

[1] Y. Kamihara, T. Watanabe, M. Hirano, and H. Hosono, J. Am. Chem. Soc. 130, 3296 (2008).

[2] Q.-Y. Wang, Z. Li, W.-H. Zhang, Z.-C. Zhang, J.-S. Zhang, W. Li, H. Ding, Y.-B. Ou, P. Deng, K. Chang, J. Wen, C.-L. Song, K. He, J.-F. Jia, S.-H. Ji, Y. Wang, L. Wang, X. Chen, X. Ma, Q.-K. Xue, Chin. Phys. Lett. **29**, 037402 (2012).

[3] W.-H. Zhang, Y. Sun, J.-S. Zhang, F.-S. Li, M.-H. Guo, Y.-F. Zhao, H.-M. Zhang, J.-P. Peng, Y. Xing, H.-C. Wang, T. Fujita, A. Hirata, Z. Li, H. Ding, C.-J. Tang, M. Wang, Q.-Y. Wang, K. He, S.-H. Ji, X. Chen, J.-F. Wang, Z.-C. Xia, L. Li, Y.-Y. Wang, J. Wang, L.-L. Wang,

M.-W. Chen, Q.-K. Xue, and X.-C. Ma, Chin. Phys. Lett. **31**, 017401 (2014).

[4] L.Z. Deng, B. Lv, Z. Wu, Y.Y. Xue, W.H. Zhang, F.S. Li, L.L. Wang, X.C. Ma, Q.K. Xue, and C.W. Chu, Phys. Rev. B **90**, 214513 (2014).

[5] J.-F. Ge, Z.-L. Liu, C. Liu, C.-L. Gao, D. Qian, Q.-K. Xue, Y. Liu, J.-F. Jia, Nat. Mater. **14**, 285 (2015).

[6] D. Liu, W. Zhang, D. Mou, J. He, Y.-B. Ou,Q.-Y. Wang, Z. Li, L. Wang, L. Zhao, S. He, Y. Peng, X. Liu, C. Chaoyu, L. Yu, G. Liu, X. Dong, J. Zhang, C. Chen, Z. Xu, J. Hu, X. Chen, Z. Ma, Q. Xue and X.J. Xhou, Nat. Comm. **3**, 931 (2012).

[7] S. He, J. He, W.-H. Zhang, L. Zhao, D. Liu, X. Liu, D. Mou, Y.-B. Ou, Q.-Y. Wang, Z. Li, L. Wang, Y. Peng, Y. Liu, C. Chen, L. Yu, G. Liu, X. Dong, J. Xhang, C. Chen, Z. Xu, X. Chen, X. Ma, Q. Xue, and X.J. Zhou, Nat. Mater. **12**, 605 (2013).

[8] R. Peng, X.P. Shen, X. Xie, H.C. Xu, S.Y. Tan, M. Xia, T. Zhang, H.Y. Cao, X.G. Gong, J.P. Hu, B.P. Xie, D. L. Feng, Phys. Rev. Lett. **112**, 107001 (2014).

[9] J.J. Lee, F.T. Schmitt, R.G. Moore, S. Johnston, Y.-T. Cui, W. Li, M. Yi, Z.K. Liu, M. Hashimoto, Y. Zhang, D.H. Lu, T.P. Devereaux, D.-H. Lee and Z.-X. Shen, Nature **515**, 245 (2014).

[10] Q. Fan, W. H. Zhang, X. Liu, Y.J. Yan, M.Q. Ren, R. Peng, H. C. Xu, B. P. Xie, J. P. Hu, T. Zhang, and D. L. Feng, Nat. Phys. **11**, 946 (2015).

[11] L. Zhao, A. Liang, D. Yuan, Y. Hu, D. Liu, J. Huang, S. He, B. Shen, Y. Xu, X. Liu, L. Yu, G. Liu, H. Zhou, Y. Huang, X. Dong, F. Zhou, Z. Zhao, C. Chen, Z. Xu, X.J. Zhou, Nat. Comm. **7**, 10608 (2016).

[12] X.H. Niu, R. Peng, H.C. Xu, Y.J. Yan, J. Jiang, D.F. Xu, T.L. Yu, Q. Song, Z.C. Huang, Y.X. Wang, B.P. Xie, X.F. Lu, N.Z. Wang, X.H. Chen, Z. Sun, and D.L. Feng, Phys. Rev. B **92**, 060504(R) (2015).

[13] Y. J. Yan, W. H. Zhang, M. Q. Ren, X. Liu, X. F. Lu, N. Z. Wang, X. H. Niu, Q. Fan, J. Miao, R. Tao, B. P. Xie, X. H. Chen, T. Zhang, D. L. Feng, Phys. Rev. B **94**, 134502 (2016).

[14] Y. Miyata, K. Nakayama, K. Suawara, T. Sato, and T. Takahashi, Nat. Mater. **14**, 775 (2015).

[15] C.H.P. Wen, H.C. Xu, C. Chen, Z.C. Huang, X. Lou, Y.J. Pu, Q. Song, B.P. Xie, M. Abdel-Hafiez, D.A. Chareev, A.N. Vasiliev, R. Peng, and D.L. Feng, Nat. Comm. **7**, 10840, (2016).

[16] Z.R. Ye, C.F. Zhang, H.L. Ning, W. Li, L. Chen, T. Jia, M. Hashimoto, D.H. Lu, Z.-X. Shen, and Y. Zhang, arXiv:1512.02526 .

[17] C.-L. Song, H.-M. Zhang, Y. Zhong, X.-P. Hu, S.-H. Ji, L. Wang, K. He, X.-C. Ma, and Q.-K. Xue, Phys. Rev. Lett. **116**, 157001 (2016).

[18] B. Lei, J.H. Cui, Z.J. Xiang, C. Shang, N.Z. Wang, G.J. Ye, X.G. Luo, T. Wu, Z. Sun, and X.H. Chen, Phys. Rev. Lett. **116**, 077002 (2016).

[19] K. Hanzawa, H. Sato, H. Hiramatsu, T. Kamiya, and H. Hosono, Proc. Nat. Acad. Sci. **113**, 3986 (2016).

[20] O.K. Andersen and L. Boeri, Annalen der Physik **523**, 8 (2011).

[21] T. Bazhirov and M.L. Cohen, J. Phys.: Condens. Matter **25**, 105506 (2013).

[22] J. He, X. Liu, W. Zhang, L. Zhao, D. Liu, S. He, D. Mou, F. Li, C. Tang, Z. Li, L. Wang, Y. Peng, Y. Liu, C. Chen, L. Yu, G. Liu, X. Dong, J. Zhang, C. Chen, Z. Xu, X. Chen, X. Ma, Q. Xue, X. J. Zhou, Proc. Nat. Acad. Sci. **111**, 18501 (2014).

[23] Q. Si and E. Abrahams, Phys. Rev. Lett. **101**, 076401 (2008).

[24] J.P. Rodriguez and E.H. Rezayi, Phys. Rev. Lett. **103**, 097204 (2009).

[25] S. Raghu, Xiao-Liang Qi, Chao-Xing Liu, D.J. Scalapino, Shou-Cheng Zhang, Phys. Rev. B **77**, 220503(R) (2008).

[26] P.A. Lee and X.-G. Wen, Phys. Rev. B **78**, 144517 (2008).

[27] I.I. Mazin, D.J. Singh, M.D. Johannes, and M.H. Du, Phys. Rev. Lett. **101**, 057003 (2008).

[28] K. Kuroki, S. Onari, R. Arita, H. Usui, Y. Tanaka, H. Kontani, and H. Aoki, Phys. Rev. Lett. **101**, 087004 (2008).

[29] J.P. Rodriguez, M.A.N. Araujo, P.D. Sacramento, Phys. Rev. B **84**, 224504 (2011).

[30] J.P. Rodriguez, M.A.N. Araujo, P.D. Sacramento, Eur. Phys. J. B **87**, 163 (2014).

[31] D.P. Arovas and A. Auerbach, Phys. Rev. B **38**, 316 (1988).

[32] C.L. Kane, P.A. Lee and N. Read, Phys. Rev. B **39**, 6880 (1989).

[33] A. Auerbach and B. E. Larson, Phys. Rev. B **43**, 7800 (1991).

[34] J.P. Rodriguez, Phys. Rev. B **82**, 014505 (2010).

[35] See Supplemental Material at ....

[36] A. Auerbach and D.P. Arovas, Phys. Rev. Lett. **61**, 617 (1988).

[37] At wavenumbers $\boldsymbol{k} = 0$ and $(\pi/a)(\hat{\boldsymbol{x}} + \hat{\boldsymbol{y}})$, the spectral weight in (5) diverges as the cSDW spin gap vanishes at the QCP. It yields the bound $\Delta_{cSDW} > k_F v_0$ that guarantees the validity of (5). Here, v_0 coincides with the velocity of cSDW spinwaves at the QCP[34]. The bound $|\boldsymbol{k} - \boldsymbol{Q}_{q_0}| > k_F$, likewise, guarantees the validity of (5) at $\boldsymbol{k}$ near cSDW wavenumbers $\boldsymbol{Q}_{q_0}$.

[38] At $t_1^{\parallel} = 0$, the convolution (4) implies intrinsic broadening of the electron bands below the Fermi level: $\Delta\omega \sim \frac{1}{8}(\epsilon_F/2s_0) = \frac{1}{2}\pi x t_1^{\perp}(\hat{\boldsymbol{x}})$ at $t \gg J$. The Goldstone mode associated with hidden magnetic order (inset to Fig. 1a) may no longer exist once $t_1^{\parallel} \neq 0$, however. In such case, the coherent and incoherent d_{yz} bands shown in Fig. 1b may experience level repulsion at cSDW momentum $(\pi/a)\hat{\boldsymbol{x}}$, likewise the d_{xz} bands at cSDW momentum $(\pi/a)\hat{\boldsymbol{y}}$.

[39] In the independent electron approximation, adding small but positive intra-orbital nearest-neighbor hopping, $0 < t_1^{\parallel} < t_1^{\perp}(\hat{\boldsymbol{x}})$, results in an electron band centered at wavenumber $(\pi/a)\hat{\boldsymbol{x}}$ for the d_{yz} orbital with mass anisotropy $m_x > m_y$. The mass anisotropy of the corresponding emergent hole band at zero 2D momentum is the reverse within the Schwinger-boson-slave-fermion mean-field approximation, at ideal hopping, $t_1^{\parallel} = 0$. Adding the mean fields $R_1^{\parallel} = \langle b^{\dagger}_{i,d\pm,s} b_{j,d\pm,s}\rangle$ and $P_1^{\parallel} = \frac{1}{2}\langle f^{\dagger}_{i,d\pm} f_{j,d\pm}\rangle$ for intra-orbital nearest-neighbor hopping of electrons (before any 90 degree spin rotations about the y axis) results in elliptical electron Fermi surface pockets at wavenumbers $(\pi/a)\hat{\boldsymbol{x}}$ and $(\pi/a)\hat{\boldsymbol{y}}$ for the d_{yz} and the d_{xz} orbitals, respectively, with the major axes along the principal axes. Both of the extra mean fields vanish in the optimized theory at large s_0, however. (Cf. ref. [30].)

[40] J.P. Rodriguez, J. Phys.: Condens. Matter **28**, 375701 (2016).

[41] X. Chen, S. Maiti, A. Linscheid and P.J. Hirschfeld, Phys. Rev. B **92**, 224514 (2015).

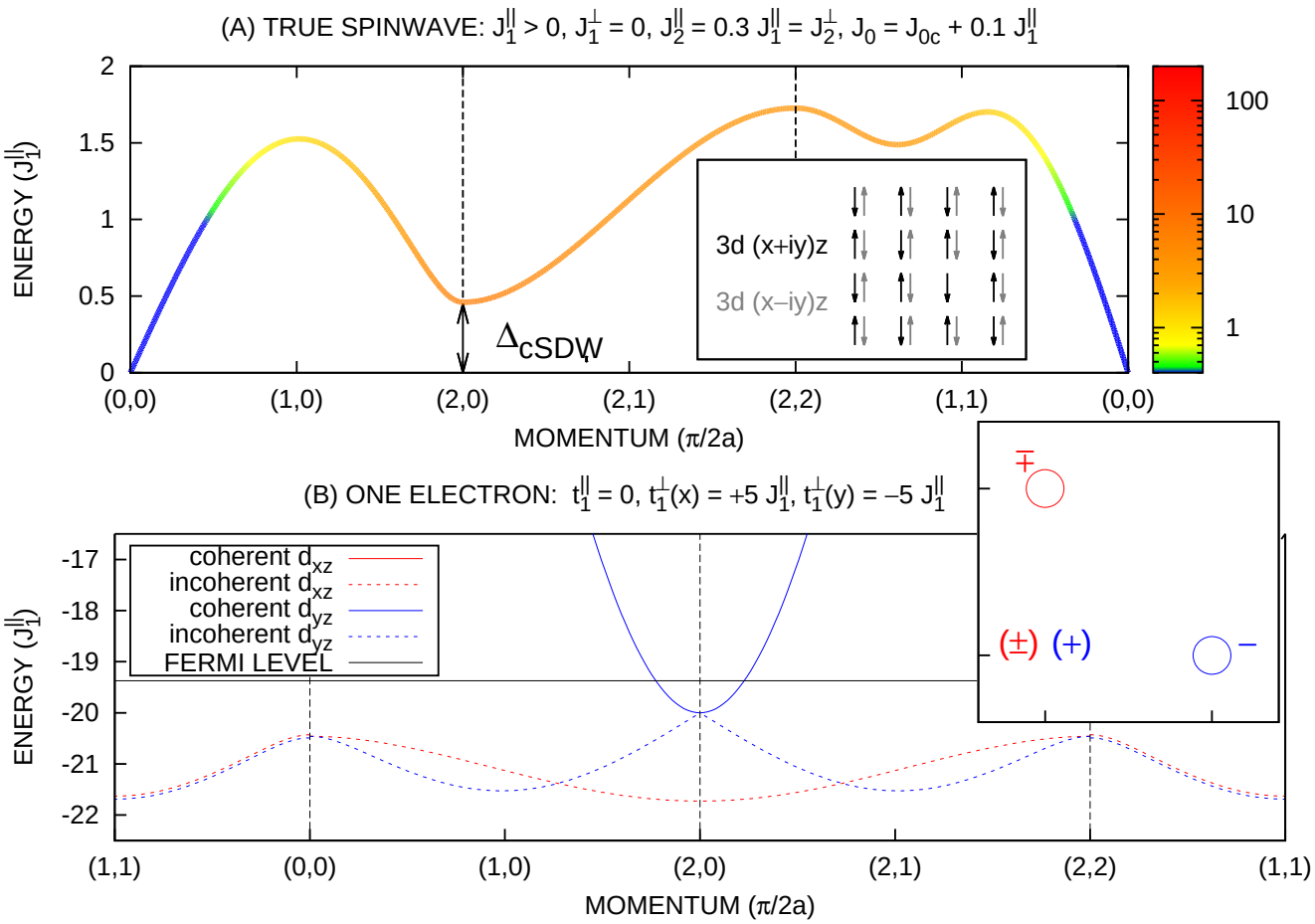

FIG. 1: (a) The imaginary part of the transverse spin susceptibility, Eq. 3, in the true spin channel and (b) the imaginary part of the one-electron propagator near half filling, Eq. 5, at site-orbital concentration $x = 0.01$. Not shown in (b) is intrinsic broadening due to the incoherent contributions in Eq. 4.

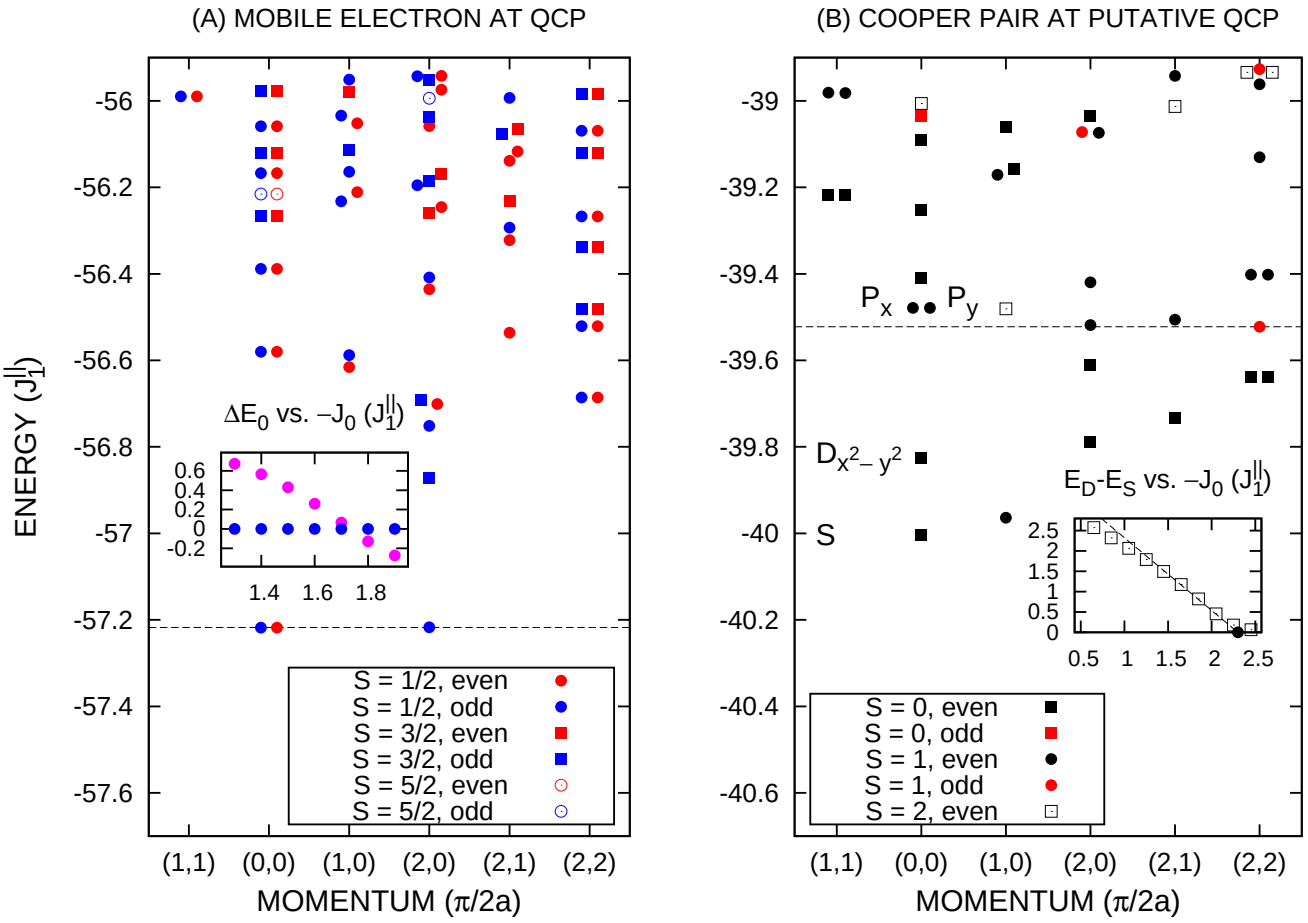

FIG. 2: (a) Low-energy spectrum of two-orbital t-J model, Eq. (1) plus constant $\frac{3}{4}(N_{\rm Fe}-1)J_0$, over a 4×4 lattice, with one electron more than half filling. Model parameters coincide with those listed by Fig. 1, except $t_1^{\|}=2\,J_1^{\|}$ and $-J_0=1.733\,J_1^{\|}$. (b) Low-energy spectrum of Eq. (1) plus repulsive interactions (see text) plus constant $\frac{1}{4}(N_{\rm Fe}-2)J_0$, but with two electrons more than half filling, with $-J_0=2.25\,J_1^{\|}$, and with $U_0'=\frac{1}{4}J_0+1000\,J_1^{\|}$. Some points in spectra are artificially moved slightly off their quantized values along the momentum axis for the sake of clarity.

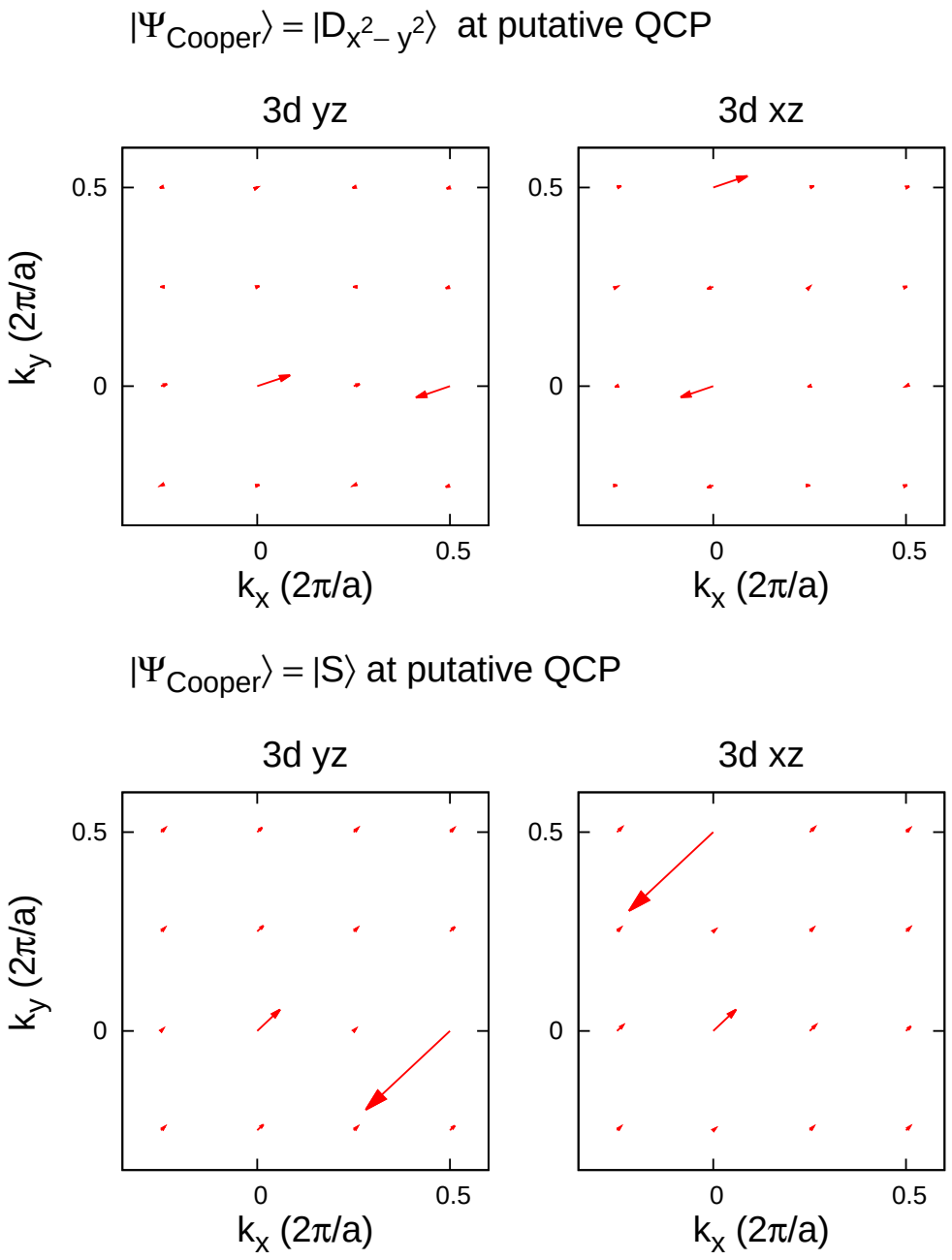

FIG. 3: The complex order parameter for superconductivity, Eq. 6, symmetrized with respect to both reflections about the principal axes.